Ni-MgO catalyst prepared by a sol-gel method for low temperature CO_2 methanation

Kaiying Wang [a], Xiaoqing He [b,c], Xinhua Liang [a,*]

[a] Department of Energy, Environmental & Chemical Engineering, Washington University in St. Louis, St. Louis, Missouri 63130, United States

[b] Electron Microscopy Core Facility, University of Missouri, Columbia, Missouri 65211, United States

[c] Department of Mechanical and Aerospace Engineering, University of Missouri, Columbia, Missouri 65211, United States

* Email: Xinhua.Liang@wustl.edu

Abstract

CO_2 methanation presents a promising route to simultaneously reduce CO_2 emissions and store renewable energy. Nickel supported on magnesium oxide (Ni-MgO) stands out as an effective catalyst for CO_2 methanation, but suffers from low activity at temperatures below 300°C. In this work, Ni-MgO prepared by a sol-gel method (Ni-MgO-SG) exhibited markedly higher activity at T ≤300°C compared to catalysts prepared by other synthesis routes. Detailed characterizations revealed that the superior performance of the Ni-MgO-SG catalyst originated from smaller Ni nanoparticle size, higher surface area, higher low- and medium-strength basic sites, and abundant surface oxygen vacancies. The smaller Ni nanoparticles provided increased exposed active surface area, while the oxygen vacancies facilitated CO_2 adsorption and activation at low temperatures. These features, combined with the intrinsic basicity of MgO and the moderate interactions between Ni and the support, led to a highly selective and stable catalyst that can

operate at low temperatures. Overall, Ni-MgO-SG shows promise for sustainable fuel production processes.

Keywords: Sol-gel method; Oxygen vacancies; Basic sites; Low temperature CO_2 methanation

1. Introduction

The escalating climate crisis has prompted the scientific community to diligently explore sustainable solutions for mitigating carbon dioxide (CO_2) emissions and transitioning towards a carbon-neutral future. Among these innovative approaches, CO_2 methanation has emerged as a promising technology that holds significant potential in addressing the dual challenges of carbon emission and renewable energy storage [1-3]. This process involves the catalytic conversion of CO_2 and hydrogen (H_2) into methane (CH_4), a versatile energy carrier and an environmentally benign alternative to conventional fossil fuels. The efficiency and selectivity of this reaction are highly dependent on the choice of catalysts, which play a crucial role in facilitating the reaction, lowering the activation energy, and determining the overall performance of the process. Several types of catalysts have been investigated for CO_2 methanation, and some of the most common ones are Ni [3-7], Co [8], Ru [9-11], Pt [12], and Rh [13] catalysts. Among these catalysts, Ni catalysts are widely used in CO_2 methanation since Ni is abundant and relatively cost-effective. Besides, Ni possesses a high catalytic activity for the dissociation of CO_2 and the subsequent hydrogenation to form methane.

Despite the advantages, challenges remain for Ni catalysts in CO_2 methanation. For instance, Ni catalysts are sensitive to carbon deposition (coking), which can inhibit their catalytic activity [14, 15]. Sintering, a prevalent mechanism of catalyst deactivation, pertains to the progressive

aggregation and coalescence of catalyst particles at elevated temperatures, leading to a diminished performance of Ni catalysts [16]. An effective strategy to mitigate sintering is to lower the reaction temperature, which also thermodynamically disfavors CO formation. Therefore, designing a catalyst with high activity at low temperatures is imperative. The catalytic performance of Ni-based CO_2 methanation catalysts strongly depends on the properties of the support material. Many substrates, including SiO_2 [17], Al_2O_3 [18, 19], CeO_2 [3], MgO [20], TiO_2 [21, 22], ZrO_2 [23, 24] and zeolite [14], have been employed for CO_2 methanation in recent years. Among these, MgO is a commonly used substrate for Ni due to its ability to form solid solutions with NiO, stemming from the comparable lattice parameters of NiO (4.17 Å) and MgO (4.21 Å) [20]. The formation of NiO-MgO solid solution facilitates various catalytic processes like hydrogenation [25], reforming [26], and syngas production [27]. The synthesis conditions significantly influence the extent of NiO-MgO solid solution formation, including calcination temperature [28], Ni loading [29], etc. The reducibility of Ni^{2+} within the solid solution also relies on the position of Ni^{2+} in the MgO lattice and metal-support interactions. Besides, the Ni-MgO interface and interactions are governed by the synthesis method. Among various synthesis techniques, sol-gel method offers control over the catalyst's structure and morphology, influencing its performance. For example, a Ni-Mg/SBA-15 synthesized by ammonia evaporation method demonstrated superior activity on CO_2 methanation compared to wetness impregnation, attributed to enhanced metal-support interactions and weakly basic hydroxyl groups [30]. The authors found that incorporating 5 wt.% Mg into phyllosilicate structures optimized medium basic site concentration, promoting formate formation and low temperature CO_2 methanation. Gracia et al. studied the effects of impregnation sequence on Ni-ZrO_2/carbon nanotube (CNT) catalyst preparation, and discovered that sequential loading of ZrO_2 followed by

Ni onto CNT supports resulted in a substantially higher CO_2 methanation performance versus co-impregnation of the Ni and ZrO_2 precursors together [31]. Characterization revealed that the co-impregnated catalyst contained NiO nanoparticles encapsulated in ZrO_2 shells. The core-shell structure restricted access to the Ni active sites and Ni-ZrO_2 interfacial regions, resulting in inferior CO_2 methanation performance compared to the sequentially impregnated catalyst. In another research, sol-gel synthesized $La_{0.5}Ce_{1.5}NiO_4$ perovskite-derived catalysts displayed an excellent 78.9% CO_2 conversion and 99.3% CH_4 selectivity at 350°C, resulting from optimized basic sites and abundant oxygen vacancies [32]. Additionally, sol-gel Ni/SiO_2 outperformed impregnation analogs for CO_2 methanation, further evidencing the synthesis-performance relationship [33]. Therefore, synthesis techniques that optimized basicity [22] and oxygen vacancy formation [34] leaded to enhanced performance in CO_2 methanation.

The presence of oxygen vacancies in metal oxide catalysts plays an important role in enhancing the catalytic activity for low temperature CO_2 methanation [35, 36]. Several studies demonstrated that increasing the concentration of oxygen vacancies in catalysts like CeO_2 and ZrO_2 led to improved CO_2 conversion and CH_4 selectivity [34, 37, 38]. The oxygen vacancies introduce localized electron-rich sites that can facilitate CO_2 activation and hydrogenation. A combination of an *in situ* DRIFTS analysis and Density functional theory (DFT) calculation have been reported to identify the role of oxygen vacancies and the change of reaction mechanism by introducing of oxygen vacancies. For example, Su et al. found that oxygen vacancies in Ni/CeO_2-La-600 catalyst facilitated the adsorption of CO_2 and its conversion to the formate (HCOO*) intermediate by reducing the energy barriers for these steps [34]. CO_2 molecules in the gas phase first adsorbed onto the Ni/CeO_2-La-600 surface and reacted with the

active O* (oxygen vacancy) to form OCO_2 * . Then, the formed OCO_2 * can further react with the dissociated H* from metallic nickel to generate hydrogenated carbonates, which can be further hydrogenated to yield HCOO*. With the introduction of oxygen vacancies, the rate-determining step shifted from the hydrogenation of adsorbed CO_2 to HCOO* (as in the case of Ni/CeO_2 without oxygen vacancies) to the decomposition of HCOO* to formyl (CHO*), which had a lower energy barrier on Ni/CeO_2-La-600 compared to Ni/CeO_2. Additionally, oxygen vacancies promoted the direct dissociation of CO_2 to CO*, which was kinetically more favorable than the HCOO* decomposition pathway. For the Ni/CeO_2-La-600 catalyst, two reaction pathways coexisted: the HCOO* pathway and the dominant direct CO* pathway. The direct CO* pathway was advantageous as it did not involve multiple thermodynamically stable intermediates. Moreover, a small portion of HCOO* dissociated to CO* and was further hydrogenated to CH_4, contributing to the overall methanation reaction. Duan et al. also found that the introduction of oxygen vacancies can change the reaction mechanism for CO_2 methanation [39]. On the Ru/CeO_2 catalyst with oxygen vacancies, the reaction followed the formate pathway, where oxygen vacancies catalyzed the dissociation of formate to methanol, which was the rate-determining step. In contrast, for the Ru/α-Al_2O_3 catalyst system without oxygen vacancies, the reaction proceeded through the CO pathway, with CO as the key intermediate. Oxygen vacancies can also be created in MgO. Several studies showed that creating oxygen vacancies in MgO further enhanced its catalytic performance [40, 41]. For instance, reduction of Ni/MgO catalysts at elevated temperatures and high H_2 concentrations promoted the reducibility of NiO species and generation of oxygen vacancies, leading to enhanced CO_2 adsorption capacity and increased CH_4 yield during CO_2 methanation [42].

In this study, MgO was selected as the catalyst support owing to its inherent basicity and ability to generate abundant oxygen vacancies. While NiO-MgO solid solutions have been widely applied, the intrinsic links between solid solution formation extent, Ni reducibility, metal-support interactions, and overall Ni-MgO catalytic performance for CO_2 methanation remain unclear. Elucidating these relationships will provide greater understanding of how to optimize Ni-MgO catalyst synthesis for the activity and stability of low temperature CO_2 methanation. To that end, a series of Ni-MgO catalysts were synthesized via various methods and characterized extensively using various techniques including TEM, XRD, H_2-TPR, CO_2-TPD, and XPS to elucidate correlations between structural properties and CO_2 methanation performance.

2. Experimental Section

2.1 Catalyst synthesis

Ni-MgO catalysts with a 10 wt.% nominal Ni loading were prepared by three synthesis methods: (i) sol-gel (SG), (ii) incipient wetness impregnation (IW), and (iii) coprecipitation (CP). For the SG method, appropriate quantities of nickel(II) nitrate hexahydrate ($Ni(NO_3)_2 \cdot 6H_2O$) and magnesium nitrate hexahydrate ($Mg(NO_3)_2 \cdot 6H_2O$) precursors were dissolved in deionized water, followed by the addition of an aqueous citric acid solution in a metal ion to citric acid molar ratio of 1:1.5. The resulting mixture was vigorously stirred at 80°C to facilitate gelation. The obtained gel was subsequently dried overnight at 130°C to acquire the precursor material as a yellow-green foam before final calcination in air at 600°C for 2 hours (2 °C/min heating rate) to yield the Ni-MgO-SG catalyst. A pure MgO was also synthesized by SG method, denoted as MgO-SG. For the IW approach, a MgO support material (Strem Chemicals, Inc.) was impregnated with an aqueous solution of $Ni(NO_3)_2 \cdot 6H_2O$ overnight before drying at 110°C and calcining in

air at 600°C for 2 hours (2 °C/min heating rate) to achieve the Ni-MgO-IW catalyst. Lastly, for the CP pathway, aqueous solutions of Ni and Mg nitrate and sodium hydroxide (NaOH) were simultaneously added dropwise into vigorously stirred water at 400 rpm while maintaining a pH of ~12. The collected precipitate was repeatedly washed with warm deionized water before drying overnight at 110°C and calcination in air at 600°C for 2 hours (2 °C/min heating rate) to obtain the Ni-MgO-CP catalyst.

2.2 Catalyst characterizations

The specific surface areas of the catalysts were determined by nitrogen adsorption/desorption isotherms at -196°C using a Quantachrome Nova 4000e automated gas sorption analyzer. Prior to analysis, the samples were outgassed at 250°C for 8 hours. Surface area values were estimated via the Brunauer–Emmett–Teller (BET) method. Powder X-ray diffraction (XRD) patterns were collected on a Bruker d8 diffractometer using Cu Kα radiation (λ = 1.5406 Å) at 40 kV and 40 mA, with a step size of 0.03° and a scanning rate of 3°/min. Inductively coupled plasma optical emission spectrometry (ICP-OES) was performed on a PerkinElmer Optima 7300DV instrument for precise measurement of nickel loadings. X-ray photoelectron spectroscopy (XPS) was conducted with a Physical Electronics 5000 VersaProbe II system equipped with an Al Kα radiation source to evaluate surface composition. Scanning and transmission electron microscopy (TEM) imaging and energy dispersive X-ray spectroscopy (EDS) elemental mapping were performed using a probe-aberration corrected Thermofisher Spectra 300 operating at 300 kV. The direct visualization of nickel nanoparticle morphologies was revealed in the STEM-high angle annular dark field (HAADF) detector with a collection angle ranging from 80 mrad to 200 mrad. Temperature-programmed reduction (H_2-TPR) profiles were obtained on a Micrometrics

AutoChem II 2920 from 100 to 900°C at 10°C/min under a 10% H_2/Ar gas mixture flowing at 50 mL/min over approximately 100 mg of sample loaded into a quartz U-tube. Thermogravimetric analysis (TGA) was performed utilizing a TGA 5500 analyzer. The analytical sample was subjected to a temperature ramp from ambient temperature to 200°C, followed by an isothermal duration at 200°C for 1 hour. Subsequently, the temperature was further ramped from 200 to 800°C at a constant heating rate of 10°C/min. A continuous airflow of 25 mL/min was maintained over the sample throughout the entire analysis. CO_2 temperature-programmed desorption (CO_2-TPD) experiments were performed in a quartz tube reactor interfaced to a QMS200 mass spectrometer (Stanford Research System) for effluent gas analysis. Prior to analysis, samples underwent in-situ reduction at 750°C with flowing hydrogen for 2 hours. Subsequently, the temperature was lowered to 50°C under helium flow to enable CO_2 adsorption for 1 hour, thereby saturating the catalyst surface. The system was then purged to eliminate weakly physiosorbed species. For the TPD analysis, the temperature was ramped from 50 to 800°C at 10°C/min under helium carrier gas, with the desorption profile continuously monitored by tracking m/z = 44, indicative of gaseous CO_2 evolution.

2.3 Catalytic performance evaluation

The catalytic activity was evaluated in a fixed-bed reactor equipped with a K-type thermocouple. Reaction temperatures ranged from 200°C to 450°C. The catalyst was sandwiched between two quartz wool layers to preclude bypassing. Prior to reaction, 100 mg of the catalyst was *in situ* reduced at 750°C for 2 hours under 50 mL/min H_2 flow. Upon cooling to 200°C, the feed gas was switched to H_2/CO_2 mixture with a H_2/CO_2 molar ratio of 4 for methanation. Catalytic performance was assessed at 50°C increments from 200-450°C with a 10°C/min heating ramp

between steps. Additional CO_2 methanation experiments were conducted under varying gas hourly space velocity (GHSV) and pressure conditions. The kinetic experiment was conducted separately using 15 mg of catalyst to maintain the CO_2 conversion below 20%. For some data sets, three repeat experiments were done, allowing for error bar calculations to be performed on the results.

The effluent stream was analyzed using a gas chromatograph (SRI Model 8610C) with a thermal conductivity detector. H_2, CO, and CH_4 were separated on a 5A molecular sieve column, while a Hayesep D column was used to quantify CO_2 and other hydrocarbons. The catalytic activity was evaluated via CO_2 conversion and CH_4 selectivity, which are defined as follows.

$$F = \frac{Q}{22400 * 60}$$

$$X_{CO2}(\%) = (F_{CO2,in} - F_{CO2,out})/ F_{CO2,in}*100\%$$

$$S_{CH4(\%)} = F_{CH4,out}/(F_{CO2,in} - F_{CO2,out})*100\%$$

where F is the molar flow rate (mol/s) and Q is the volume flow rate (mL/min). The stability of catalysts was examined by keeping track of the conversion and selectivity evolution by a time-on-stream test over a considerable period of 200 hours at 300°C under a GHSV of 36 $L \cdot g^{-1} \cdot h^{-1}$. The formula for the turnover frequency (TOF) is displayed as follows.

$$TOF(s^{-1}) = X_{CO2} * F_{CO2,\,in} * S_{CH4} * \frac{M_{Ni}}{m_{cat} * w * D_{Ni}}$$

where M_{Ni} represents the atomic mass of Ni, m_{cat} is the mass of the catalyst, w is the proportion of Ni in the catalyst, and D_{Ni} represents the Ni particle dispersion, which is estimated from TEM results of reduced samples [43]. The carbon balance is calculated as follows:

$$\text{Carbon balance} = \frac{F_{CO2,out} + F_{CO,out} + F_{CH4,out}}{F_{CO2,in}} * 100\%$$

During the test, carbon balances exceeded 98% across all tests.

3. Results and Discussion

3.1. Catalyst characterizations

XRD was utilized to examine the crystal structures of the Ni-MgO catalysts prepared via different synthetic methods. For the purpose of comparison, NiO and MgO were also included. As shown in Fig. 1, MgO and NiO not only exhibited similar diffraction patterns but also showed nearby characteristic peaks because both NiO and MgO have similar ionic radii and the same rock salt structure [44]. The diffraction peak positions for the fresh Ni-MgO samples are nearly identical across all samples. The observed 2θ values at 36.9°, 42.8°, 62.2°, 74.5°, and 78.4° correspond to the (111), (200), (220), (311), and (222) planes of the face-centered cubic (fcc) MgO phase, respectively [45]. Given the close similarities between NiO and MgO diffraction patterns, the XRD signals for MgO and Ni-MgO solid solutions normally overlap with those of NiO. However, the absence of any doublet peaks indicates successful formation of the Ni-MgO solid solution [46]. While peak positions showed negligible variation among samples, significant differences were discerned in peak width. As an example, Ni-MgO-SG exhibited substantial broadening of the (200) peak, compared to the other catalysts, indicative of smaller crystalline domains. Application of the Debye-Scherrer equation enabled quantification of the average crystalline size, with results summarized in Table 1. As anticipated, Ni-MgO-SG possessed the smallest crystallite size of 7.6 nm. For the reduced Ni-MgO-IW and Ni-MgO-CP samples, two distinct peaks corresponding to the cubic nickel reflections at 44° and 52° were observed (JCPDF 87-0712), indicative of the formation of crystalline nickel phases [47]. In contrast, the reduced Ni-MgO-SG sample did not exhibit detectable nickel reflections, suggesting a highly

dispersed nature of the nickel species within this catalyst. Furthermore, an increase in the crystallite size was observed for all reduced samples, with the Ni-MgO-CP sample exhibiting the most significant growth from 10.8 nm to 39.5 nm. The Ni-MgO-IW and Ni-MgO-SG samples experienced more moderate increases, from 10.7 nm to 17.9 nm and 7.6 nm to 15.4 nm, respectively. These observations highlight the influence of the synthesis method on the dispersion and crystallite size of the nickel species, which can ultimately impact the catalytic performance.

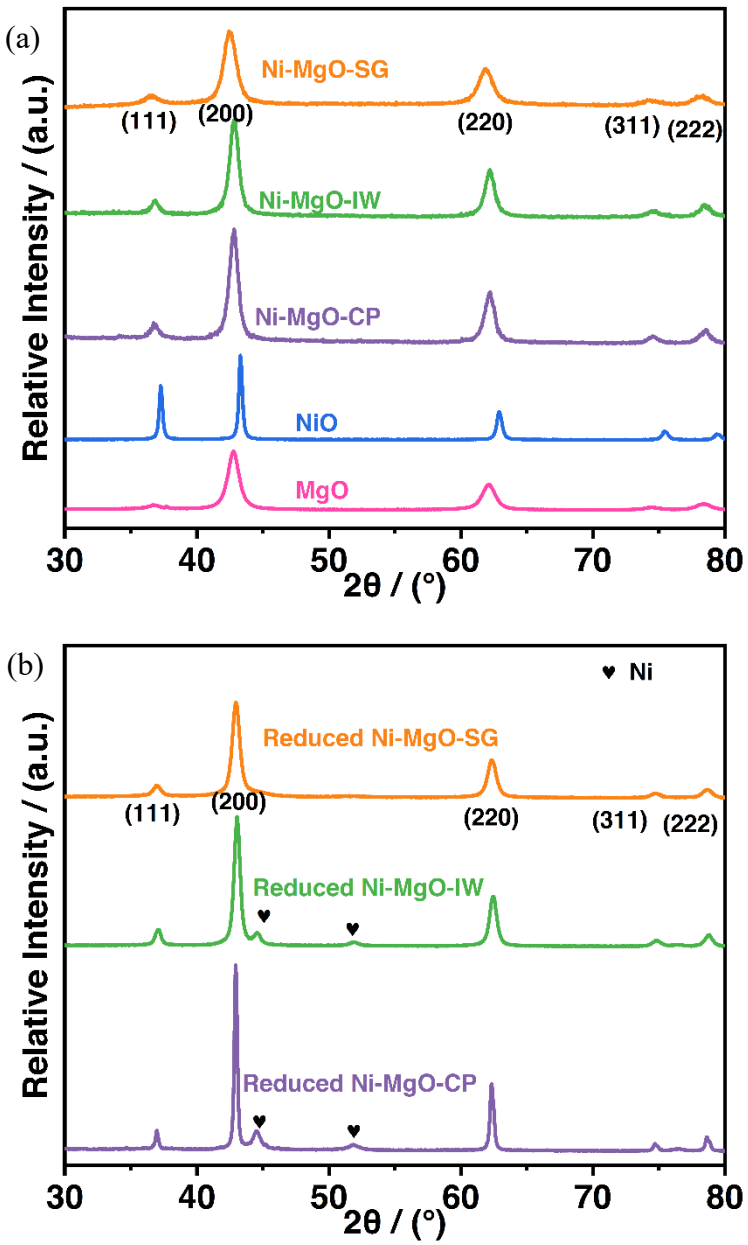

Fig. 1 XRD patterns of (a) fresh and (b) reduced Ni-MgO catalysts prepared by different methods.

The textural properties of the catalyst samples were characterized by nitrogen adsorption analysis at -196°C. The Brunauer-Emmett-Teller (BET) specific surface areas, pore volumes, and Barret–Joyner–Halenda (BJH) average pore diameters are summarized in Table 1. The Ni loadings of

the synthesized catalysts as measured by ICP-OES are also shown in Table 1, with the obtained compositions aligning closely with the nominal values targeted during catalyst preparation. Fig. 2 displays the nitrogen adsorption/desorption isotherms of the synthesized catalysts, with the inset showing the pore size distributions calculated from the BJH method. Notably, the Ni-MgO-SG catalyst exhibited the highest specific surface area, approximately twice that of the other samples. According to the International Union of Pure and Applied Chemistry (IUPAC) classification, the isotherms corresponded to Type IV with H3 hysteresis loops in the 0.6-0.9 relative pressure range, indicative of nitrogen capillary condensation in mesopores (2-50 nm) [48]. As for the pore size, the Ni-MgO-IW, Ni-MgO-SG and Ni-MgO-CP catalysts showed narrow pore size distributions centered at 3.2 nm, 4.1 nm, and 13.9 nm, respectively. These results demonstrated that the preparation method significantly impacted the textural properties of the synthesized catalysts. The higher surface area of Ni-MgO-SG can provide more sites for CO_2 adsorption and activation, which would be advantageous for methanation. Previous study showed that MgO with a high surface area had higher CO_2 adsorption capacity than MgO with a low surface area [49]. The enhanced CO_2 uptake and dissociative ability of Ni-MgO-SG was evidenced by subsequent CO_2-TPD analysis, where the Ni-MgO-SG sample demonstrated the highest CO_2 adsorption capacity and ability to dissociate adsorbed CO_2 species at low temperatures.

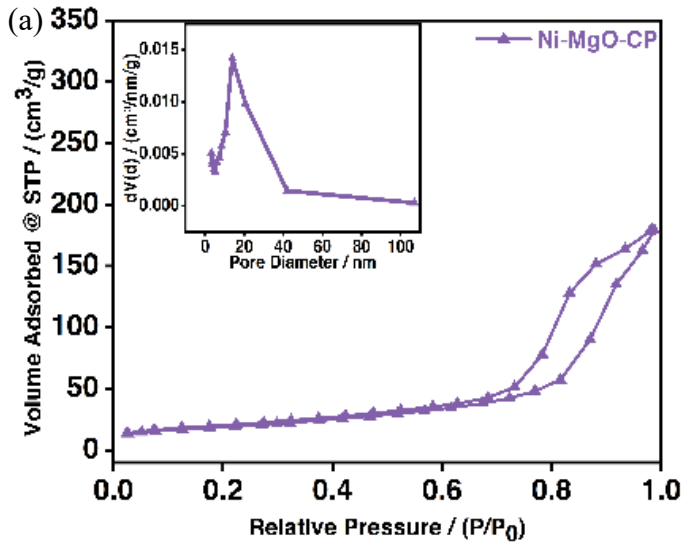
(a)
Ni-MgO-CP
Volume Adsorbed @ STP / (cm3/g)
Relative Pressure / (P/P0)
dV(d) / (cm3/nm/g)
Pore Diameter / nm

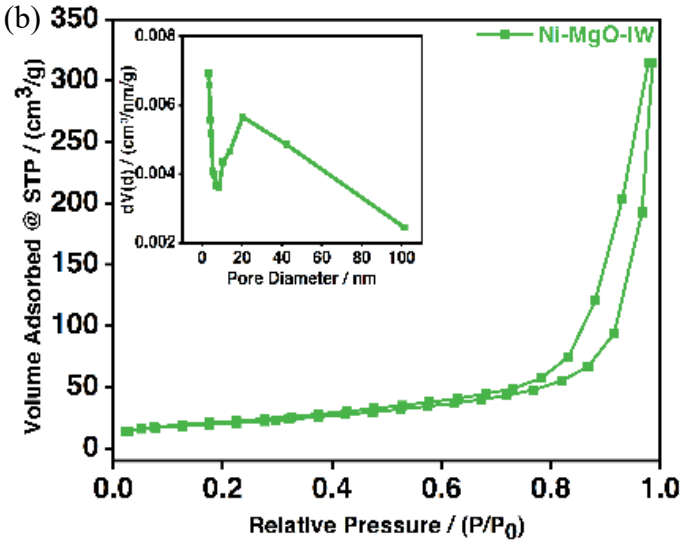
(b)
Ni-MgO-IW
Volume Adsorbed @ STP / (cm3/g)
Relative Pressure / (P/P0)
dV(d) / (cm3/nm/g)
Pore Diameter / nm

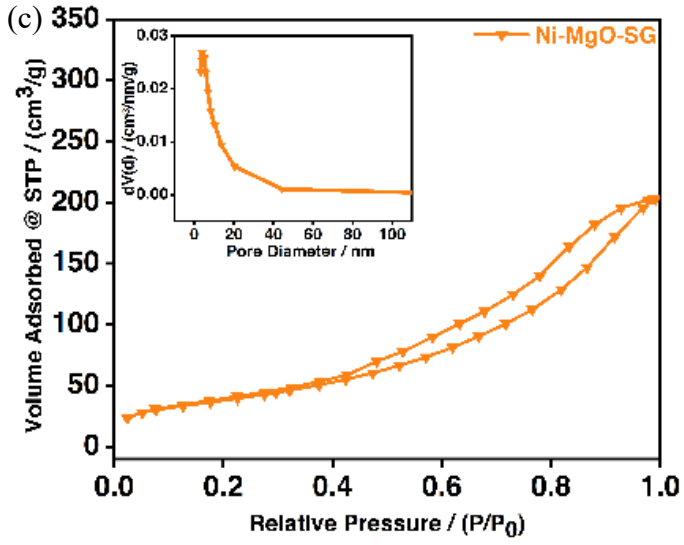
(c)
Ni-MgO-SG
Volume Adsorbed @ STP / (cm3/g)
Relative Pressure / (P/P0)
dV(d) / (cm3/nm/g)
Pore Diameter / nm

Fig. 2 Nitrogen adsorption–desorption isotherm of (a) Ni-MgO-CP, (b) Ni-MgO-IW, and (c) Ni-MgO-SG. The inset shows the pore size distribution obtained from the BJH method.

Table 1. Physical properties of the obtained catalysts.

Sample IDs	Ni loading (wt.%)	BET Surface area (m^2/g)	Pore Volume (cm^3/g)	Average pore diameter (nm)	Crystallite size (fresh) (nm)	Crystallite size (reduced) (nm)	Crystallite size (spent) (nm)
Ni-MgO-IW	9.9	71	0.48	3.3	10.7	17.9	21.2
Ni-MgO-CP	9.7	67	0.27	13.9	10.8	39.5	39.5
Ni-MgO-SG	9.8	139	0.31	4.1	7.6	15.4	16.5

H_2-TPR profiles of the synthesized catalysts are presented in Fig. 3. Pure NiO exhibited a solitary reduction peak around 370°C, aligning with reported literature values [28, 50, 51]. Additionally, both commercially obtained and sol-gel synthesized MgO samples did not demonstrate hydrogen consumption under the tested experimental conditions. For Ni-MgO systems, Ni-MgO-IW and Ni-MgO-SG exhibited clear, well-resolved dual peaks, while Ni-MgO-CP displayed an asymmetric single peak. According to previous studies, the first centered peak around 450°C corresponded to the reduction of Ni oxide at the outermost and subsurface

layers of the MgO lattice, and the second peak near 750°C corresponded to Ni reduction within the solid solution bulk [28, 44, 52]. As shown in Fig. 3a, Ni-MgO-SG exhibited a higher reduction temperature than Ni-MgO-IW, indicating a stronger interaction between Ni and MgO. Among the tested catalysts, Ni-MgO-CP showed the strongest interaction between Ni and MgO. To better understand the reduction behavior, deconvoluted H_2-TPR peaks are shown in Fig. S1, with the deconvolution analysis summarized in Table S1. As can be seen from Table S1, most Ni species across catalysts were reduced at temperatures higher than 700°C, indicative of the formation of Ni-MgO solid solution. However, the proportion of easily reduced Ni species greatly impacted CO_2 methanation activity at low temperature. Here, we defined the percentage of 1st peak area as the proportion of easily reduced Ni species. According to Fig. 3b, Ni-MgO-SG possessed higher easily reducible Ni species (24%) versus Ni-MgO-CP (9%), correlating with its superior methanation performance. To facilitate a comprehensive comparison among these three catalysts, the quantification of hydrogen consumption was also provided. Specifically, the hydrogen consumption for Ni-MgO-SG in reducing nickel oxide at the outermost and subsurface layers of the MgO lattice, as well as in reducing nickel within the solid solution bulk, was 15.3 cm^3/g and 44.9 cm^3/g, respectively. In the case of Ni-MgO-IW, the corresponding values were 6.8 cm^3/g and 32.1 cm^3/g. Notably, Ni-MgO-CP exhibited a mere 0.2 cm^3/g consumption in reducing nickel oxide at the outermost and subsurface layers of the MgO lattice, while a substantial 141.3 cm^3/g of hydrogen was consumed in reducing nickel within the solid solution bulk. The percentage of readily reducible nickel species for Ni-MgO-SG (25%) and Ni-MgO-IW (17%) closely aligned with the values obtained from the deconvolution analysis, which were 24% and 15%, respectively. Thus, a greater population of low-temperature reducible Ni species facilitated CO_2 activation and was beneficial for methanation. It is worth noting that the “ideal”

homogeneous solid solutions are non-reducible at up to 900°C [53]. Therefore, the reduction behavior in this study corresponds to the partial reduction of Ni from non-homogeneous Ni-MgO phases.

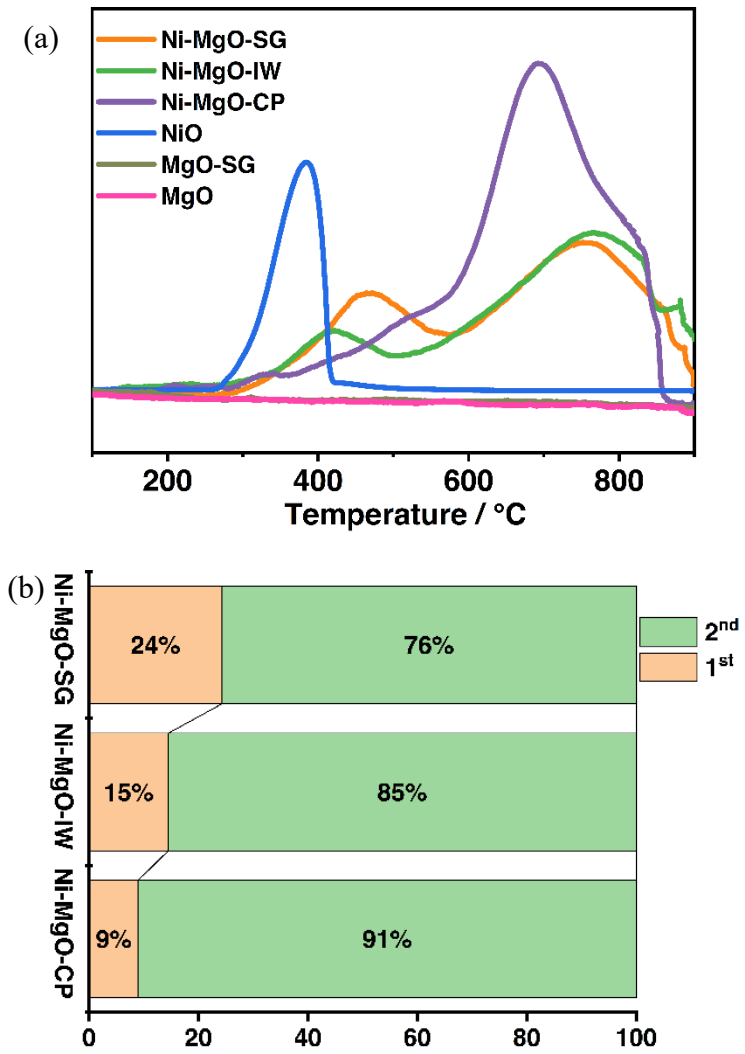

Fig. 3 (a) H_2-TPR profiles of NiO, MgO, MgO-SG, Ni-MgO-CP, Ni-MgO-IW, and Ni-MgO-SG, and (b) the distribution of Ni species for the obtained Ni-MgO catalysts.

The morphology of the prepared catalysts was analyzed by TEM. As shown in Fig. 4a, the fresh prepared Ni-MgO-SG sample contained uniformly distributed Ni particles with an average particle size at 5.0±0.8 nm. Conversely, it was difficult to find exposed Ni particles for the Ni-

MgO-CP and Ni-MgO-IW samples, as shown in Fig. S2. The Ni particles were closely wrapped by MgO. Energy-dispersive X-ray spectroscopy (EDS) mapping confirmed the presence of 9.22±1.08 wt.% and 9.26±1.52 wt.% Ni for Ni-MgO-CP and Ni-MgO-IW, respectively, aligning with the ICP-OES results in Table 1. Different morphologies of the prepared samples were in line with the H_2-TPR profiles from Fig. 3, where Ni-MgO-SG sample contained the most abundant reducible Ni species while Ni-MgO-CP and Ni-MgO-IW samples contained less reducible Ni species. For the fresh prepared Ni-MgO-SG sample, several black dots were observed under high-resolution transmission electron microscopy (HRTEM) as indicated by the circles in Fig. 4b. The yellow circled area was further investigated by atomic resolution STEM-HAADF imaging to identify the nature of the dark dots shown in the HRTEM image. Ni single atom and/or its clusters were clearly observed to be anchored to the MgO substrate and/or incorporated into MgO lattice. The reason for the formation of single atom sites may come from comparable lattice parameters of NiO (4.17 Å) and MgO (4.21 Å). Ni-MgO solid solution could serve as an effective strategy to achieve Ni single atoms, which was proved by some previous studies [20, 54, 55]. The obvious single atom catalysts were only observed in Ni-MgO-SG sample, which also indicated the importance of choosing the suitable synthesis method. However, Ni single atom catalysts favored the generation of CO in CO_2 methanation. The Ni atoms preferentially located on the surface of the MgO favored low-coordinated sites. These anchored, isolated Ni entities were capable of activating CO_2 via the reverse water-gas shift reaction. However, further hydrogenation of the CO intermediates to methane or methanol necessitated larger metallic Ni ensembles [20]. So, these Ni single atoms cannot be the active centers. To verify that, the TEM images of the Ni-MgO-SG sample after the pretreatment were collected. As can be seen from Fig. 4d, the Ni single atoms disappeared after a 750°C reduction

under hydrogen flow. This phenomenon was consistent with previous studies where high anneal temperature causing the sintering of metal single atoms [54, 56]. The reduced Ni-MgO-SG sample still exhibited a small particle size of 6.1±0.8 nm. This value was even lower than the fresh Ni-MgO-CP and Ni-MgO-IW grain sizes obtained from XRD. An examination of the reduced Ni-MgO-CP and Ni-MgO-IW catalysts revealed a broader distribution of nickel particle sizes in comparison to Ni-MgO-SG. As depicted in Fig. S3, the reduced Ni-MgO-CP exhibited a nickel particle size range of 5-30 nm, with a mean size of 17.2 nm. Similarly, the reduced Ni-MgO-IW displayed a size distribution ranging from 5-20 nm, with a mean size of 11.2 nm. Notably, the average particle sizes for both Ni-MgO-CP and Ni-MgO-IW were larger than those observed for Ni-MgO-SG. Furthermore, the particle size distributions for Ni-MgO-CP and Ni-MgO-IW were less uniform, compared to Ni-MgO-SG. These observations suggest that the sol-gel method facilitated the confinement of nickel species within the MgO matrix, thereby suppressing the sintering of nickel species more effectively than the conventional impregnation and co-precipitation techniques employed for Ni-MgO-CP and Ni-MgO-IW, respectively. The confined Ni species resisted sintering, and along with the enhanced reducibility, contributed to Ni-MgO-SG's superior catalytic performance and stability.

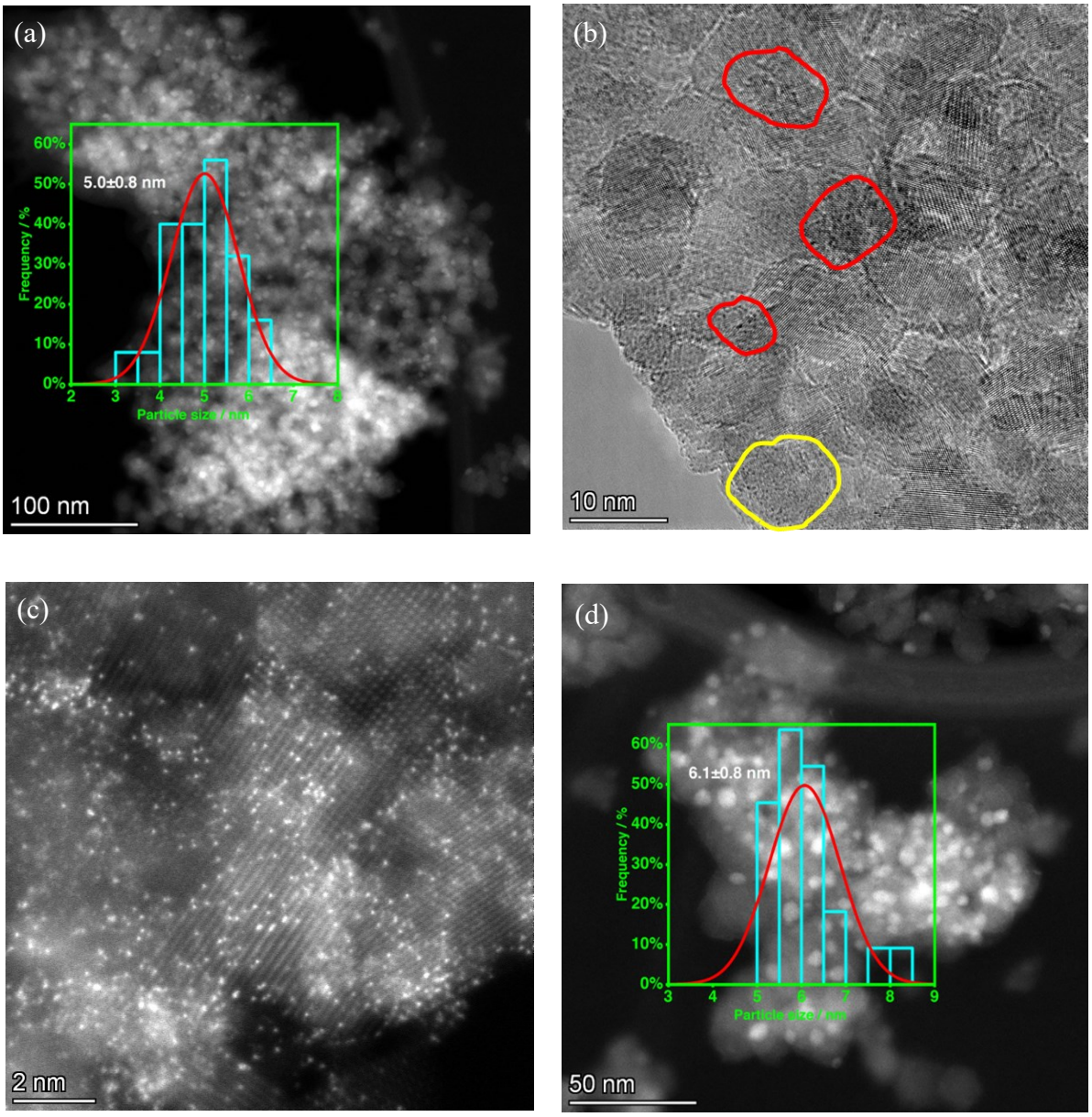

Fig. 4 (a) STEM-HAADF image of freshly prepared Ni-MgO-SG catalyst with inset showing particle size distribution histogram, (b) HRTEM image of freshly prepared Ni-MgO-SG, (c) Atomic resolution STEM-HAADF image from the region indicated by the yellow circle in image (b) showing Ni single atom and its clusters, (d) STEM-HAADF image of Ni-MgO-SG after reduction at 750°C for 2 hours under H_2 flow with inset showing particle size distribution histogram.

Fig. 5 displays the Ni 2p and O 1s XPS spectra for the synthesized catalyst samples. The Ni 2p spectra of all fresh samples exhibited a peak at approximately 855.1 eV, attributable to Ni^{2+}, and a shake-up satellite peak around 860.9 eV, consistent with reported values [37]. No metallic nickel was observed, since all the catalysts were calcinated at 600°C in air. In the O 1s spectra, two peaks were observed, one peak at ~529.3 eV associated with lattice oxygen (O_{latt}) and the other peak at ~531.4 eV associated with surface-adsorbed oxygen species (O_{surf}) [34]. Noteworthy, the surface oxygen consists of the hydroxyl oxygen and the exposed oxygen defects on the surface, which is closely associated with the catalytic surface reaction. Specifically, oxygen species including hydroxyls and oxygen vacancies present on catalyst surfaces have been shown to facilitate CO_2 adsorption and activation under reaction conditions. The lower coordination and increased protrusion of oxygen atoms that situate on vertices, steps, and kinks enables interaction with the electron-deficient carbon atom of CO_2. This allows the formation of transient carbonate intermediates, effectively anchoring CO_2 molecules to the catalyst surface. Compared to more embedded lattice oxygen, which exhibits higher coordination within the bulk structure, these unique low-coordination oxygen defects constitute the active sites for catalytic turnover [57]. As depicted in Fig. 5b, the percentage of O_{surf} species on the catalysts followed the following trend: Ni-MgO-IW (45.79%) < Ni-MgO-CP (47.87%) < Ni-MgO-SG (70.15%). This suggests that the sol-gel prepared sample could generate more oxygen vacancies and thus provided more active adsorbed oxygen species. The abundant oxygen vacancies generated in the Ni-MgO-SG catalyst significantly contributed to its enhanced CO_2 methanation performance at low temperature.

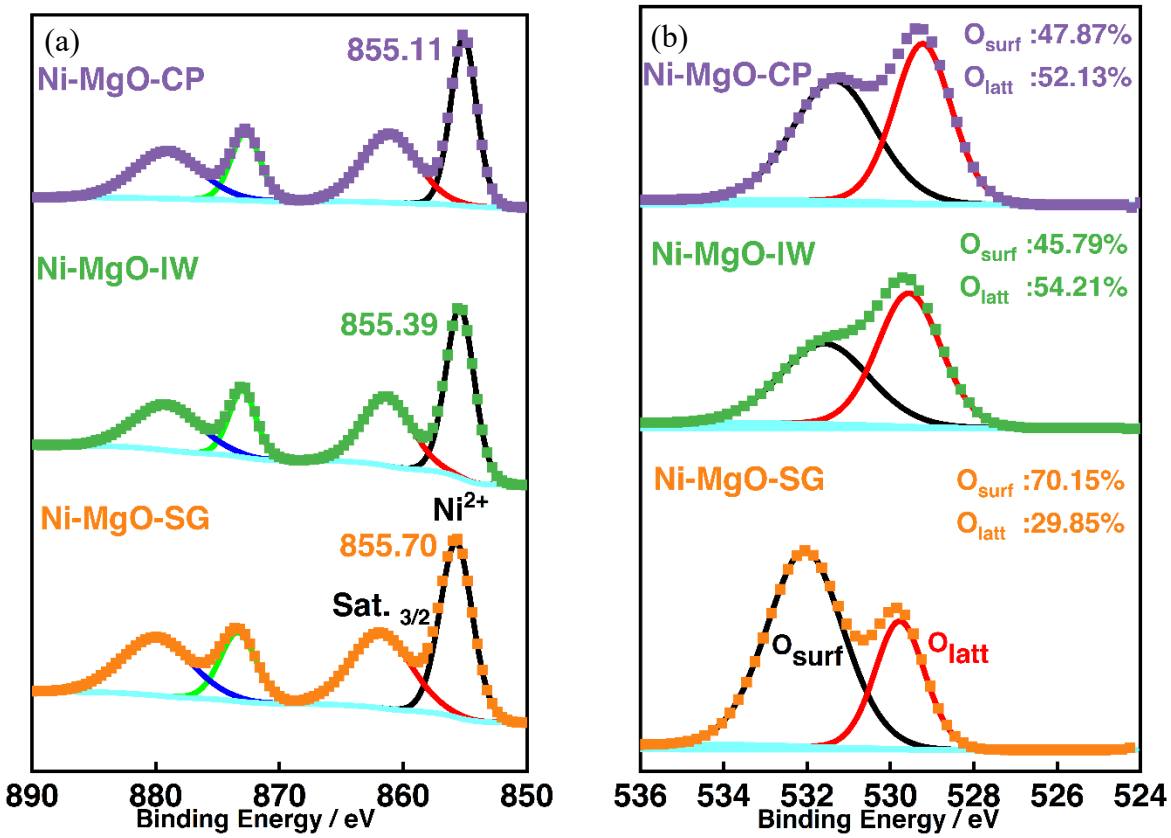

Fig. 5 XPS spectra of (a) Ni 2p and (b) O 1s of different catalysts.

CO_2-TPD was used to identify the basic site strength and distribution. As shown in Fig. 6a, the catalysts contained basic sites of varying strengths, classified as weak (50-200°C), medium (200-450°C), and strong (450-800°C) sites based on the CO_2 desorption temperatures [58]. The weak sites probably rose from Mg^{2+} sites or unreduced Ni species present in the solid solution support [45]. It is notable that the CO_2-TPD profiles for MgO and Ni-MgO samples exhibited remarkable similarities. Specifically, the Ni-MgO-IW sample displayed a CO_2-TPD profile analogous to that of the commercially obtained MgO. Similarly, the Ni-MgO-SG sample exhibited a CO_2-TPD profile comparable to that of the MgO prepared via the sol-gel method. These observations suggest that the CO_2 adsorption behavior of the Ni-MgO catalysts is primarily governed by the nature of the MgO support. For quantification, the total basic sites of Ni-MgO-CP were

normalized to 1, with deconvolution of its CO_2-TPD profile provided in Fig. S4 as an example. Fig. 6b summarizes the semi-quantitative results. Clearly, the basic site distributions dependent on synthetic methods. According to literature, weak and medium basic sites promoted CO_2 adsorption and dissociation on Ni-based catalysts [45]. CO_2 adsorbed on strong basic sites exhibited high binding energy, precluding desorption at low temperatures, and limiting the contribution of these sites to CO_2 activation for low temperature methanation. For example, Ni-MgO-CP possessed the fewest weak and medium sites, limiting its CO_2 activation below 300°C during methanation testing. In contrast, Ni-MgO-SG had over twice as many weak and medium sites versus Ni-MgO-CP, partially explaining its superior activity at low temperature. The sequence of weak and medium site percentages (Ni-MgO-SG > Ni-MgO-IW > Ni-MgO-CP) directly correlated with the order of CO_2 conversion performance. In summary, abundant weak and medium basic sites are crucial for optimizing low temperature CO_2 adsorption and activation in CO_2 methanation catalysts.

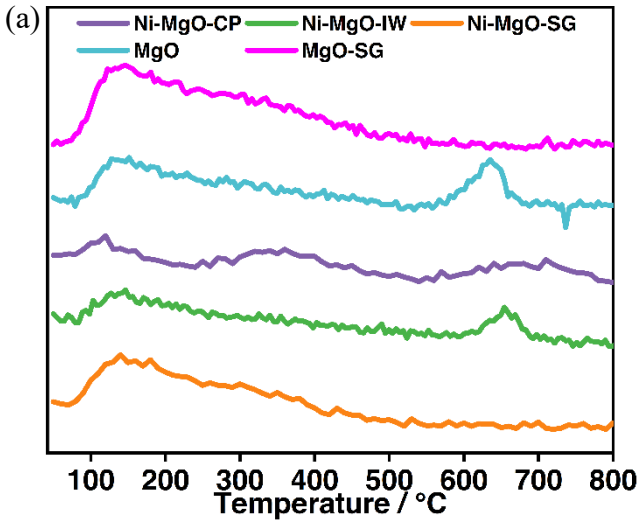

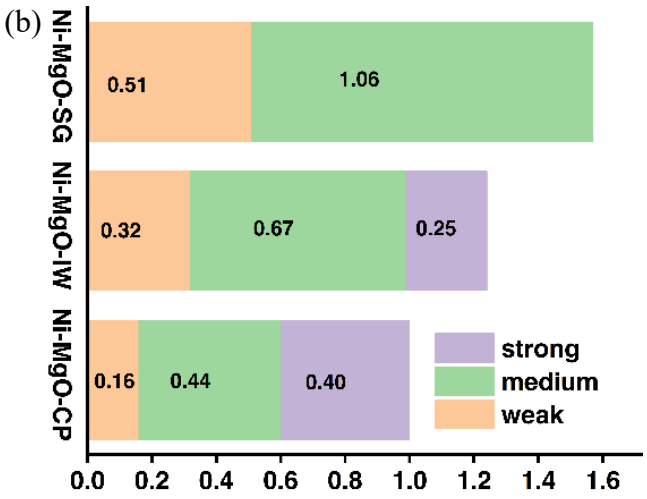

Fig. 6 (a) CO_2-TPD profiles of reduced MgO, MgO-SG, Ni-MgO-CP, Ni-MgO-IW, and Ni-MgO-SG, and (b) semi-quantitative CO_2 adsorption evaluation of catalysts based on CO_2-TPD. For comparison and evaluation of basicity of catalysts, the total amount of basic sites of Ni-MgO-CP was normalized to 1.

3.2. Catalytic performance in CO_2 methanation

Fig. 7a illustrates the CO_2 conversion from 200 to 450°C for Ni-MgO catalysts synthesized via different methods. All catalysts displayed a similar trend, with CO_2 conversion increasing from 200 to 350°C, then decreasing from 400 to 450°C, constrained by thermodynamic equilibrium limitations. Except for Ni-MgO-CP as shown in Fig. S4, which displayed a 97% selectivity towards CH_4, all other catalysts exhibited nearly 100% selectivity for CH_4 production. For CO_2 methanation, Ni-MgO-SG outperformed all other catalysts across the tested temperature range, especially below 300°C. The T_{50} of Ni-MgO-SG (273°C) was 20°C lower than Ni-MgO-CP (293°C). As evidenced in Fig. 7b, Ni-MgO-SG achieved 2% CO_2 conversion at 200°C, rapidly increasing to 22% at 250°C, whereas Ni-MgO-CP showed no conversion at 200°C and only 5.7% at 250°C. Catalysts prepared by IW also surpassed Ni-MgO-CP but underperformed

relative to Ni-MgO-SG. TOF_{CO2} provides insights into the intrinsic activity of the catalysts. The obtained TOF_{CO2} values for Ni-MgO-SG, Ni-MgO-IW, and Ni-MgO-CP were 0.15 s^{-1}, 0.12 s^{-1}, and 0.06 s^{-1}, respectively. The superior performance exhibited by Ni-MgO-SG can be attributed to its smaller nickel particle size of 6.1 nm, compared to 11.2 nm and 17.2 nm for the Ni-MgO-IW and Ni-MgO-CP samples, respectively. Previous research has demonstrated that smaller particle sizes facilitated an improved distribution of nickel particles, and highly dispersed nickel species promoted efficient hydrogen dissociation, generating an abundance of surface-dissociated hydrogen species [24]. These surface hydrogen species play a crucial role in mitigating the formation of surface nickel carbonyls, thereby effectively enhancing the low-temperature activity for CO_2 methanation. A comparative evaluation of the catalytic performance of representative nickel-based catalysts for the CO_2 methanation reaction is presented in Table S2. The current Ni-MgO-SG sample exhibited a noteworthy catalytic activity among the catalysts listed, positioning itself as a promising candidate for this reaction. In summary, comprehensive comparison of all synthetic methods revealed Ni-MgO-SG as the optimal catalyst formulation for enhanced CO_2 methanation at low temperature.

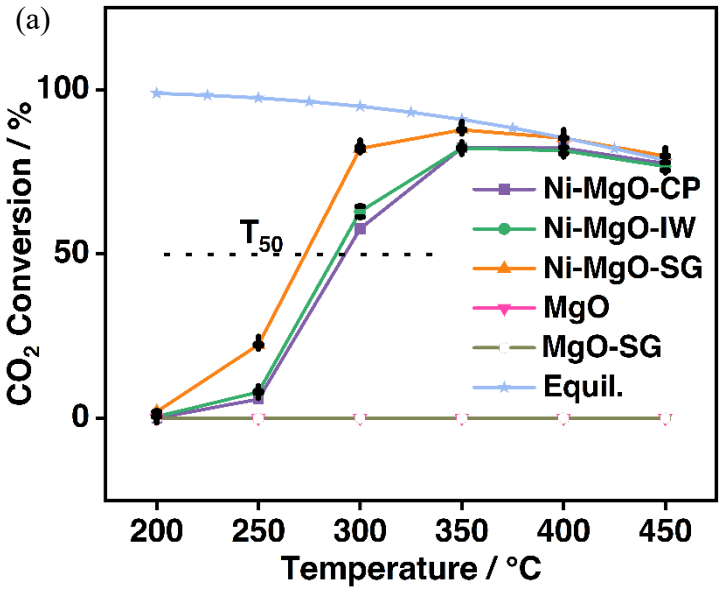

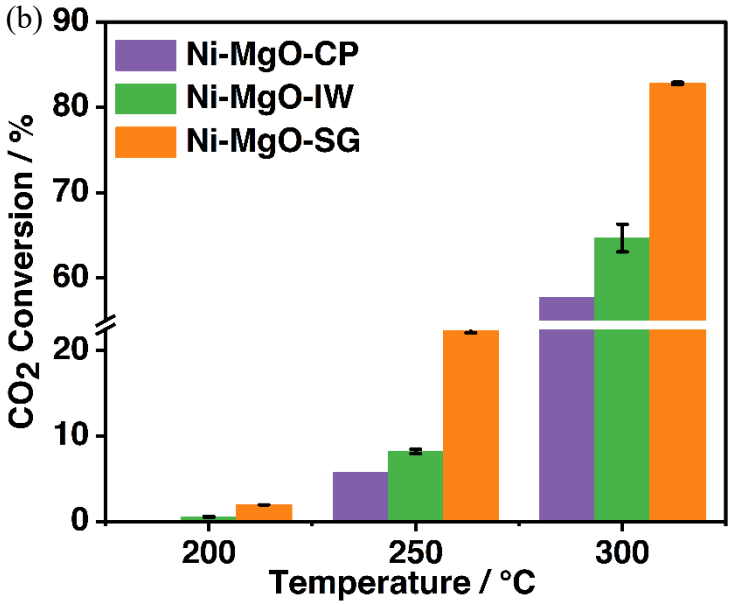

Fig. 7 (a) Effects of temperature (200-450°C) on CO_2 conversion under 14.5 psi and GHSV of 9 $L \cdot g^{-1} \cdot h^{-1}$, and (b) comparation of low temperature (200-300°C) performance of Ni-MgO catalysts.

Due to its superior performance, Ni-MgO-SG was selected to investigate the effects of pressure and GHSV on CO_2 methanation. As shown in Fig. 8, under constant pressure, CO_2 conversion decreased with increasing GHSV from 9 to 36 $L \cdot g^{-1} \cdot h^{-1}$, likely due to the shorter residence time at higher GHSV. Pressure also significantly impacted CO_2 methanation, especially over the range of 14.5-150 psi. For instance, at 9 $L \cdot g^{-1} \cdot h^{-1}$, CO_2 conversion rose from 82.6% to 94.9% when increasing pressure from 14.5 psi to 150 psi. The positive influence of elevated pressure was even more pronounced at higher GHSV, with conversion increasing from 72.3% to 90.6% over the same pressure range at 18 $L \cdot g^{-1} \cdot h^{-1}$. However, further increasing pressure from 150 psi to 300 psi only marginally improved conversion, from 94.9% to 95.6% at 9 $L \cdot g^{-1} \cdot h^{-1}$, as the reaction began to approach thermodynamic equilibrium limitations. In summary, both GHSV and pressure demonstrated notable effects on CO_2 methanation over Ni-MgO-SG, with higher

pressure significantly enhancing conversion, especially for operation at high gas hourly space velocities.

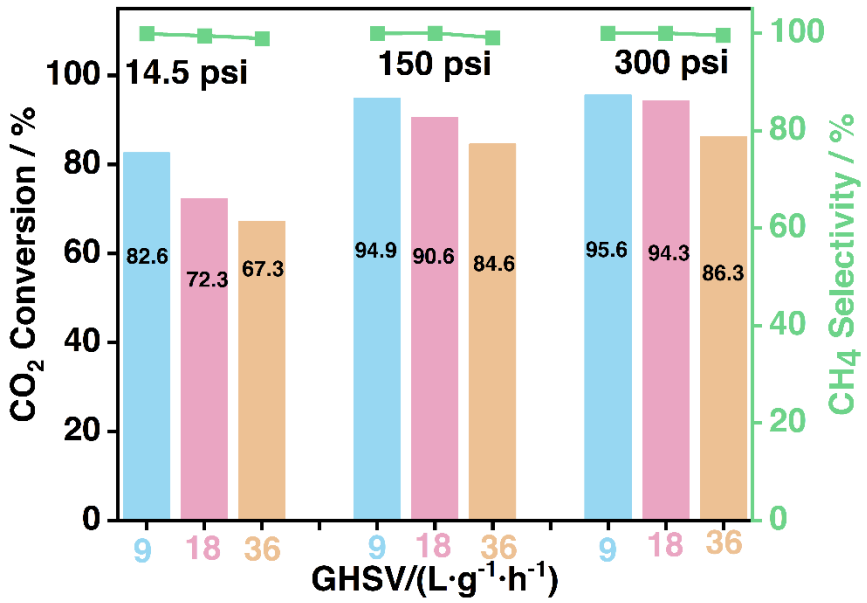

Fig. 8 CO_2 conversion and CH_4 selectivity using Ni-MgO-SG catalyst under different values of pressure and GHSV at 300°C.

The apparent activation energies (Ea) of the Ni-MgO catalysts were determined from Arrhenius plots. The CO_2 conversion was maintained below 20% during the kinetic experiment. The Ea for CO_2 methanation, calculated from the Arrhenius plots in Fig. 9a over Ni-MgO-CP, Ni-MgO-IW, and Ni-MgO-SG, are 108.4±2.3, 107.4±2.4, and 94.2±1.6 kJ/mol, respectively. These Ea values are consistent with literature values reported for other Ni-based catalysts, including 75-118 kJ/ mol for Ni/γ-Al_2O_3 [18, 59], 53.5-113 kJ/ mol for Ni/CeO_2 [60, 61], and 94-116 kJ/ mol for Ni-MgO [62, 63]. Of the tested Ni-MgO catalysts, Ni-MgO-SG exhibited the lowest Ea at 94.2±1.6 kJ/mol, indicating the lowest CO_2 activation energy barrier and the highest reaction rate. This aligned with the experimental results in Fig. 7, showing that Ni-MgO-SG had the highest

catalytic activity. In contrast, Ni-MgO-CP had the highest Ea at 108.4±2.3 kJ/mol and the lowest catalytic activity.

The stability test for the Ni-MgO-SG sample was conducted at a high GHSV of 36 $L \cdot g^{-1} \cdot h^{-1}$ at 300°C for 200 hours. As shown in Fig. 9b, the CH_4 selectivity was above 99% in the tested conditions, while the CO_2 conversion dropped slightly from ~67% to ~65%. The high stability came from the formation of Ni-MgO solid solution, which was also conformed with previous research [27, 64-66]. For example, the Ni-MgO catalyst exhibited excellent stability for the CO_2 reforming of CH_4 reaction when operated at 790°C with a GHSV of 60 $L \cdot g^{-1} \cdot h^{-1}$ for 120 hours [65]. In another research, a Mo-modified Ni-MgO catalyst also displayed excellent stability for the CO_2 reforming of CH_4 under comparable conditions of 800°C and a GHSV of 60 $L \cdot g^{-1} \cdot h^{-1}$, with stable performance observed over 850 hours on stream [27]. In our case, TEM imaging of the Ni-MgO-SG sample after stability testing in Fig. 9c revealed Ni nanoparticles remaining uniformly distributed, with a slight particle size increase from 6.1 nm to 8.9 nm. More TEM images with different magnifications for Ni-MgO-SG sample after stability testing are shown in Fig. S6. TGA was utilized to quantify carbon deposition on the spent Ni-MgO-SG catalyst after 200 hours of stability testing. The results are presented in Fig. 9d. Prior to analysis, the catalysts underwent a 200°C preheating for 1 hour to eliminate moisture. During subsequent temperature ramping from 200 to 800°C, the mass of the Ni-MgO-SG catalyst decreased from 96.6 wt.% to 95.7 wt.%, indicative of 0.9 wt.% carbonaceous residue detection. This minor coke accumulation suggests the Ni-MgO solid solution effectively inhibited coke formation. This enhanced stability is attributed to facile reaction of CO_2 adsorbed on the MgO support with deposited carbon, coupled with strong metal-support interactions preserving the Ni dispersion [64].

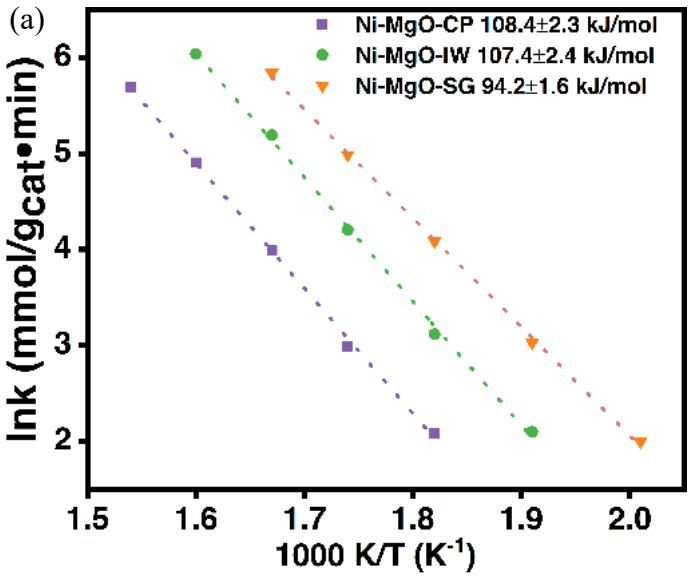
(a)
Ni-MgO-CP 108.4±2.3 kJ/mol
Ni-MgO-IW 107.4±2.4 kJ/mol
Ni-MgO-SG 94.2±1.6 kJ/mol
lnk (mmol/gcat•min)
6
5
4
3
2
1.5
1.6
1.7
1.8
1.9
2.0
1000 K/T (K-1)

(b)

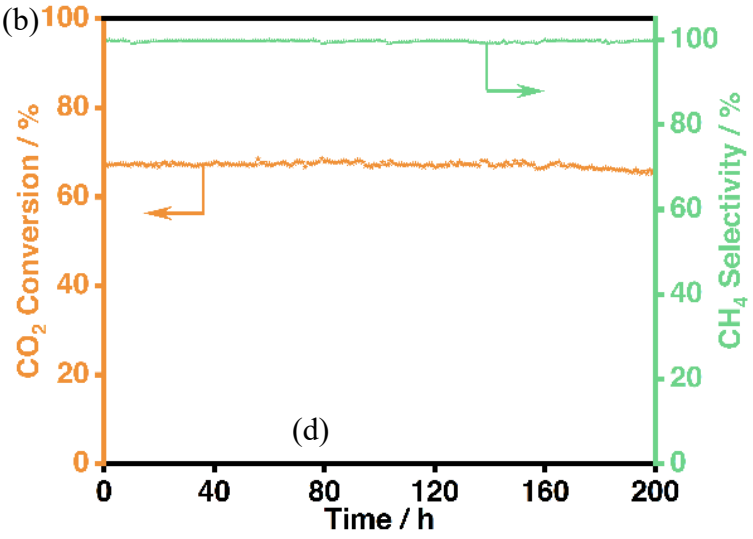
100
80
60
40
20
0
CO_2 Conversion / %
100
80
60
40
20
0
CH_4 Selectivity / %
0
40
80
120
160
200
Time / h

(d)

(c)

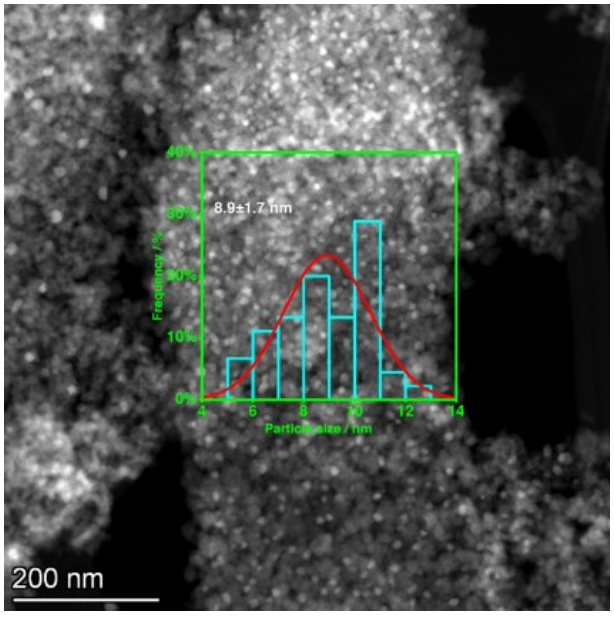
8.9±1.7 nm
Frequency / %
Particle size / nm
200 nm

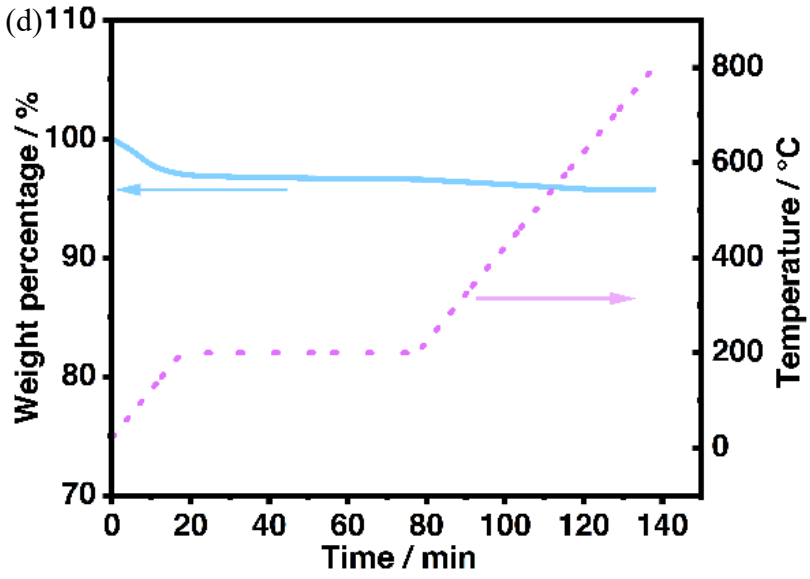

Fig. 9 (a) Arrhenius plot of Ni-MgO catalysts for CO_2 methanation, (b) stability test of Ni-MgO-SG catalyst in CO_2 methanation at 300°C and 36 $L \cdot g^{-1} \cdot h^{-1}$, (c) a representative STEM-HAADF image of Ni-MgO-SG after 200 hours' stability test, and (d) TGA profiles of Ni-MgO-SG after 200 hours' stability test.

3.3. Characterizations of spent catalysts

The spent catalysts were subjected to XRD analysis to examine the evolution of crystallite size during the reaction. As depicted in Fig. 10, a notable observation for the Ni-MgO-SG sample was the emergence of two distinct peaks corresponding to the cubic nickel reflections at 44° and 52°, albeit broad and weak in intensity. For the Ni-MgO-IW and Ni-MgO-CP samples, these two peaks appeared sharper compared to their reduced counterparts, indicating an increase in nickel particle size. Quantitative analysis of the XRD data revealed an increase in the crystallite size from 15.4 nm to 16.5 nm for the Ni-MgO-SG catalyst, while the Ni-MgO-IW catalyst exhibited an increase from 17.9 nm to 21.2 nm. In the case of the Ni-MgO-CP sample, the crystallite size remained constant at 39.5 nm, which was the same as the reduced Ni-MgO-CP sample. To

further investigate the structural evolution of the Ni-MgO-SG catalyst, TEM analysis was performed on the spent sample, as shown in Fig. 11. The TEM micrographs revealed that the nickel particles remained uniformly distributed, with an average particle size of 7.1 nm. This observation indicates a slight increase in the nickel particle size from 6.1 nm in the reduced catalyst to 7.1 nm after the reaction. The combination of XRD and TEM analyses provided valuable insights into the structural changes occurring during the catalytic reaction, particularly the increase in nickel particle size. While the Ni-MgO-SG catalyst exhibited the most significant resistance to particle growth, with a modest increase in crystallite and particle size, the Ni-MgO-IW and Ni-MgO-CP catalysts experienced more pronounced sintering effects, as evidenced by the sharper nickel reflections and larger crystallite sizes.

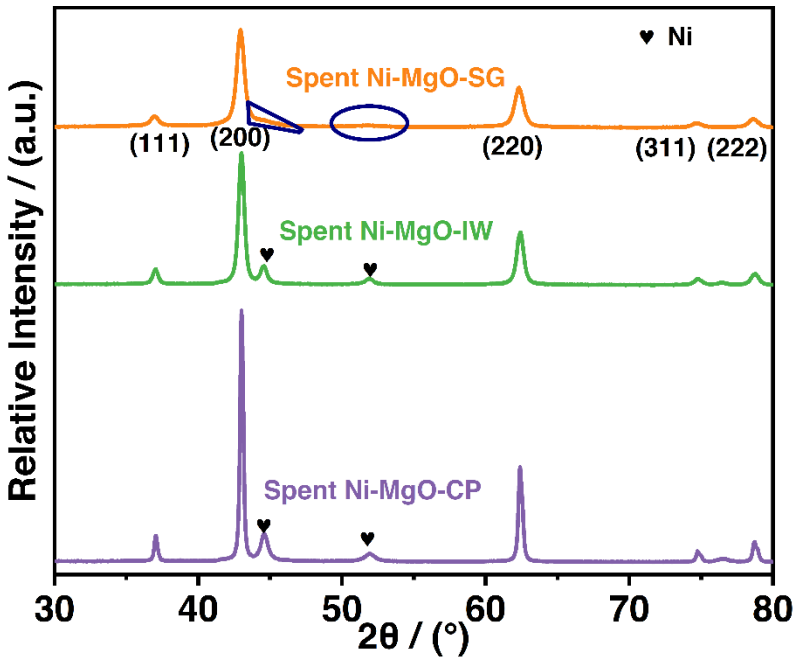

Fig. 10 XRD patterns of spent Ni-MgO-CP, Ni-MgO-IW, and Ni-MgO-SG catalysts.

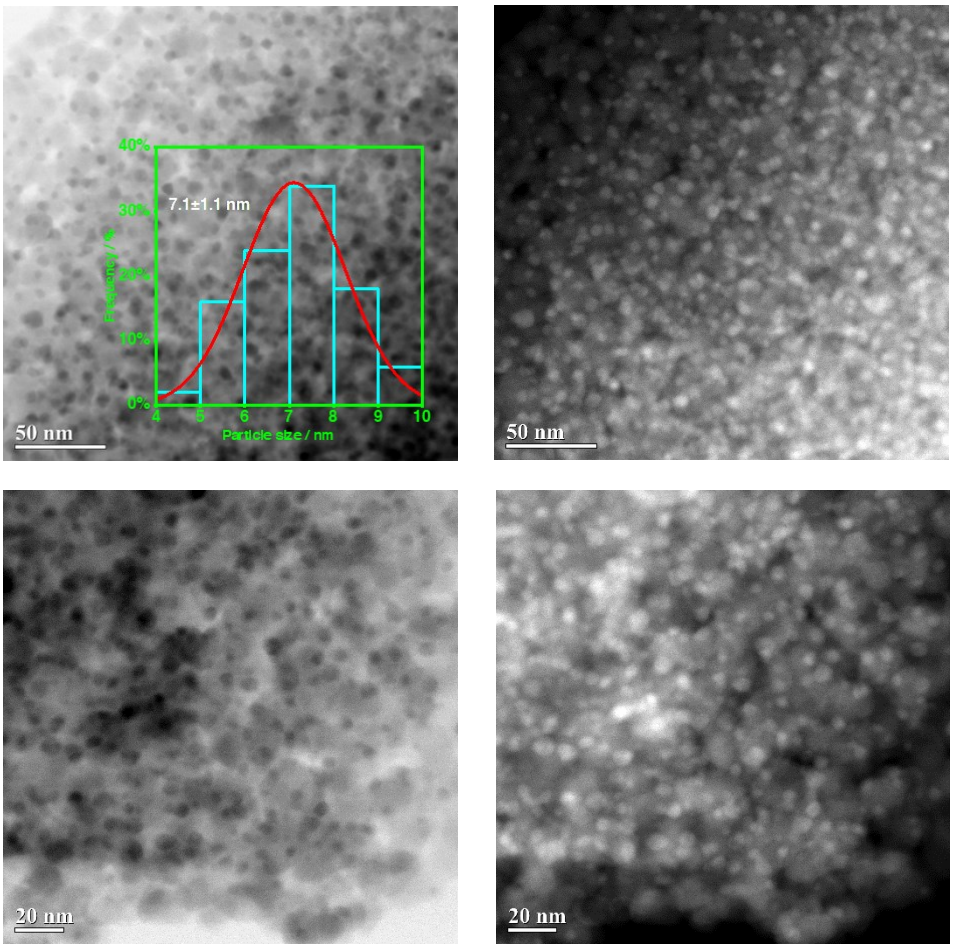

Fig. 11 STEM images of spent Ni-MgO-SG catalyst with inset showing particle size distribution histogram.

3.4. Discussions

In the present work, a Ni-MgO catalyst exhibiting both high activity and excellent stability at low temperature was synthesized via a sol-gel method for the reaction of CO_2 methanation. The sol-gel technique offers advantages of mild preparation conditions, production of high surface area nanoparticles, and uniform distribution of metal species. Besides high surface area, the abundance of oxygen vacancies played another important role in low temperature CO_2 methanation. In recent years, significant research efforts have focused on developing robust

catalysts with tunable oxygen vacancy concentrations as a strategy to enhance CO_2 conversion efficiency [34, 41, 42]. The ability to regulate the number and distribution of oxygen vacancies allows control over the adsorption and activation of reactant molecules during CO_2 conversion reactions. The advent of advanced synthetic techniques and the rational design of suitable catalyst supports have enabled precise tuning of oxygen vacancy concentrations in catalyst materials. In this work, the sol-gel synthesized Ni-MgO-SG catalyst exhibited greater oxygen vacancy concentration compared to the impregnated Ni-MgO-IW and coprecipitated Ni-MgO-CP analogs, as quantified by XPS analysis. This enhanced oxygen defect density translated to superior low temperature CO_2 methanation performance under 300°C for Ni-MgO-SG, with a 20°C lower T_{50} and 3-fold higher site-time-yield at 250°C than that of conventional synthetic protocols. The localized electrons and favorable adsorption sites provided by abundant vacancies facilitate CO_2 activation and conversion at mild temperatures.

Moreover, the reducibility of Ni^{2+} ions in a Ni-MgO solid solution plays a pivotal role in CO_2 methanation reactivity. The extent of Ni^{2+} reduction and associated catalytic performance is known to depend strongly on factors such as: i) the Ni dispersion within the MgO structure, ii) specific positioning of Ni^{2+} dopants in MgO lattice sites, and iii) the resultant metal-support interactions in the Ni-MgO system [67]. Indeed, judicious control over preparation conditions (calcination temperature, Ni loading, etc.) can effectively tune the Ni-MgO solid solution characteristics as well as the nickel-support interactions. The trends in CO_2 methanation reactivity observed in the present work correlate well with such established frameworks regarding the structure-function relationships for Ni-MgO catalysts. Based on the H_2-TPR profiles, the reducibility of Ni^{2+} varied markedly between different synthetic protocols; the sol-

gel derived Ni-MgO-SG catalyst exhibited the highest population (~24%) of readily reduced Ni^{2+} species. In contrast, lower proportions (~15% and ~9%) of easily reduced Ni^{2+} sites were identified over the Ni-MgO-IW and Ni-MgO-CP samples, respectively. Complementary TEM provided further evidence of a more homogeneous Ni entity dispersion achieved in Ni-MgO-SG, whereas Ni species encapsulation by the MgO support phase was observed for Ni-MgO-IW and Ni-MgO-CP. For Ni/MgO catalysts, metallic Ni is the active site and MgO acts as the promoter for CO_2 methanation reaction [5]. The role of Ni on the reaction is not only to decompose H_2 to H atom but also the active site for CO_2 hydrogenation steps [42, 68, 69]. In the present study, the active phase is also metallic Ni. To substantiate this, the Ni-MgO-SG sample was reduced at various temperatures (450°C, 600°C, and 750°C) and evaluated its performance in CO_2 methanation. The results can be found on Fig. S7. Among the tested temperatures, the sample reduced at 750°C exhibited the highest CO_2 conversion, indicating an enhanced activity by exposing more metallic Ni phase. Consequently, Ni-MgO-SG displayed the highest activity in CO_2 methanation, consistent with its superior Ni^{2+} reducibility.

Achieving high methane selectivity is a crucial consideration for the practical application of CO_2 methanation catalysts. At atmospheric pressure, the reduction of CO_2 primarily yields CH_4 via the CO_2 methanation pathway and/or CO via the reverse water-gas shift (RWGS) reaction. It is generally accepted that the desorption behavior of CO determines the selectivity in this process: if CO desorption is favorable, the dominant pathway is RWGS; otherwise, hydrogenation of CO to CH_4 is more likely to occur [70]. In this context, the appropriate structural and electronic modifications resulting from the strong metal-support interaction (SMSI) facilitate the generation of metal-support interfaces conducive for CO_2 adsorption and activation. Furthermore, SMSI

promotes electron transfer from the oxide substrate to the metallic nanoparticles, enhancing the adsorption strength of CO on metal sites. This phenomenon promotes the hydrogenation of CO to CH_4 rather than its desorption as a product, thereby increasing the rate of CO_2 conversion and CH_4 selectivity. In the case of our Ni-MgO system, the strong interaction between the metal and support, as evidenced from H_2-TPR analysis, contributed to achieving high selectivity toward CH_4. Another effective strategy to control methane selectivity is optimizing the reaction temperature. The Sabatier reaction is highly exothermic, and consequently, a low temperature range of 200 to 450°C is favorable for driving the reaction forward. Temperature plays a pivotal role in determining product selectivity, as it influences the desorption of reaction intermediates. At excessively low temperatures, the activation of the highly stable CO_2 molecules becomes limited, hindering their conversion to CH_4. Conversely, at elevated temperatures, methane production can be impeded due to several factors: (1) The thermodynamic equilibrium of the methanation reaction shifts toward the reactants, rendering the reaction unfavorable. (2) The endothermic RWGS reaction becomes dominant, leading to a decrease in CH_4 selectivity by promoting the formation of CO as a byproduct. In this study, the Ni-MgO-SG catalyst exhibited high activity in CO_2 methanation at temperatures $\leqslant$ 300°C, resulting in low CO selectivity within this temperature range.

Although the sol-gel synthesized Ni-MgO-SG catalyst exhibited superior low-temperature CO_2 methanation activity, a significant challenge is the requirement for high temperature (750°C) reduction pretreatments prior to catalytic testing. Such harsh activation conditions originate from strong metal-support interactions, which hinder efficient Ni^{2+} reduction. One promising strategy to mitigate these limitations, as evidenced in our previous work, is the incorporation of

secondary promoters such as CeO_2 [71] and ZrO_2 [72] to facilitate reducibility of the active phase. For instance, atomic layer deposition of CeO_2 onto Ni/Al_2O_3 catalysts was shown to enhance Ni^0 metallic character during reduction and achieve stable, high-performance bi-reforming reactivity of methane [71]. Analogous improvements were reported by Guo et al. wherein Ce addition to Ni/MgO promoted easy reducibility of the Ni phase and abundant oxygen vacancy formation, giving rise to superior catalytic activity and stability in dry reforming of methane [73]. Building off these encouraging precedents, future work should explore Ni-MgO-SG derivatives co-modified with CeO_2 or other promoters to unlock the outstanding low-temperature CO_2 methanation reactivity under milder pretreatment and operating regimes.

4. Conclusions

This work demonstrates that the preparation method significantly impacts the performance of Ni-MgO catalysts for low temperature CO_2 methanation. Of the synthesis techniques investigated, sol-gel fabrication led to a Ni-MgO catalyst with markedly higher activity at temperatures $\leq$300°C, compared to incipient wetness impregnation and coprecipitation routes. Detailed characterizations revealed that the superior low temperature performance of Ni-MgO-SG originated from several advantageous properties enabled by the sol-gel synthesis. These include smaller Ni nanoparticle size providing increased metal surface area, abundant surface oxygen vacancies facilitating CO_2 activation, and high concentration of low- and medium-strength basic sites for CO_2 adsorption. Coupled with the intrinsic basicity and moderate Ni-MgO interactions of the optimized sol-gel formulation, Ni-MgO-SG exhibited high selectivity, stability, and capability for CO_2 methanation at the mild temperatures, which are critical for the practical production of renewable CH_4. Overall, this work established synthesis-structure-performance

relationships in Ni-MgO catalysts, demonstrating sol-gel fabrication as an effective approach to enhance low temperature CO_2 methanation activity through tailored textural properties and creation of oxygen vacancies.

Conflicts of interest

There are no conflicts to declare.

Acknowledgements

This study was financially supported in part by National Science Foundation grant NSF 2306177. The authors acknowledge the use of Spectra 300 TEM at the electron microscopy core at University of Missouri.

References

[1] U. Ulmer, T. Dingle, P.N. Duchesne, R.H. Morris, A. Tavasoli, T. Wood, G.A. Ozin, Fundamentals and applications of photocatalytic CO(2) methanation, Nat. Commun., 10 (2019) 3169.
[2] Z. Liu, X. Gao, B. Liu, Q. Ma, T.-s. Zhao, J. Zhang, Recent advances in thermal catalytic CO_2 methanation on hydrotalcite-derived catalysts, Fuel, 321 (2022) 124115.
[3] Y. Xie, J. Chen, X. Wu, J. Wen, R. Zhao, Z. Li, G. Tian, Q. Zhang, P. Ning, J. Hao, Frustrated Lewis Pairs Boosting Low-Temperature CO_2 Methanation Performance over Ni/CeO_2 Nanocatalysts, ACS Catal., 12 (2022) 10587-10602.
[4] Z. Boukha, A. Bermejo-López, B. Pereda-Ayo, J.A. González-Marcos, J.R. González-Velasco, Study on the promotional effect of lanthana addition on the performance of hydroxyapatite-supported Ni catalysts for the CO_2 methanation reaction, Appl. Catal. B, 314 (2022) 121500.
[5] J. Huang, X. Li, X. Wang, X. Fang, H. Wang, X. Xu, New insights into CO_2 methanation mechanisms on Ni/MgO catalysts by DFT calculations: Elucidating Ni and MgO roles and support effects, J. CO_2 Util., 33 (2019) 55-63.
[6] A.I. Tsiotsias, N.D. Charisiou, C. Italiano, G.D. Ferrante, L. Pino, A. Vita, V. Sebastian, S.J. Hinder, M.A. Baker, A. Sharan, N. Singh, K. Polychronopoulou, M.A. Goula, Ni-noble metal bimetallic catalysts for improved low temperature CO_2 methanation, Appl. Surf. Sci., 646 (2024).
[7] W.K. Fan, M. Tahir, H. Alias, A.R. Mohamed, Catalytic CO_2 hydrogenation to produce methane over NiO/TiO_2 composite: Effect of TiO_2 structure, Int. J. Hydrogen Energy, 51 (2024) 462-478.
[8] Z. Liu, X. Gao, B. Liu, W. Song, Q. Ma, T.-s. Zhao, X. Wang, J.W. Bae, X. Zhang, J. Zhang, Highly stable and selective layered Co-Al-O catalysts for low-temperature CO_2 methanation, Appl. Catal. B, 310 (2022) 121303.
[9] X. Liu, C. Xing, F. Yang, Z. Liu, Y. Wang, T. Dong, L. Zhao, H. Liu, W. Zhou, Strong Interaction over Ru/Defects-Rich Aluminium Oxide Boosts Photothermal CO_2 Methanation via Microchannel Flow-Type System, Adv. Energy Mater., 12 (2022) 2201009.
[10] Y. Li, Z. Liu, Z. Rao, F. Yu, W. Bao, Y. Tang, H. Zhao, J. Zhang, Z. Wang, J. Li, Z. Huang, Y. Zhou, Y. Li, B. Dai, Experimental and theoretical insights into an enhanced CO_2 methanation mechanism over a Ru-based catalyst, Appl. Catal. B, 319 (2022) 121903.
[11] M. Gao, J. Zhang, P. Zhu, X. Liu, Z. Zheng, Unveiling the origin of alkali metal promotion in CO_2 methanation over Ru/ZrO_2, Appl. Catal. B, 314 (2022) 121476.
[12] X. Shi, Y. Huang, Y. Bo, D. Duan, Z. Wang, J. Cao, G. Zhu, W. Ho, L. Wang, T. Huang, Y. Xiong, Highly Selective Photocatalytic CO_2 Methanation with Water Vapor on Single-Atom Platinum-Decorated Defective Carbon Nitride, Angew. Chem., Int. Ed. Engl., 134 (2022) e202203063.
[13] A. Solis-Garcia, T.A. Zepeda, J.C. Fierro-Gonzalez, Spectroscopic evidence of the simultaneous participation of rhodium carbonyls and surface formate species during the CO_2 methanation catalyzed by ZrO_2-supported Rh, Appl. Catal. B, 304 (2022) 120955.
[14] S.N. Bukhari, C.C. Chong, H.D. Setiabudi, Y.W. Cheng, L.P. Teh, A.A. Jalil, Ni/Fibrous type SBA-15: Highly active and coke resistant catalyst for CO_2 methanation, Chem. Eng. Sci., 229 (2021) 116141.

[15] D. Schmider, L. Maier, O. Deutschmann, Reaction Kinetics of CO and CO_2 Methanation over Nickel, Ind. Eng. Chem. Res., 60 (2021) 5792-5805.
[16] M. Guo, G. Lu, The effect of impregnation strategy on structural characters and CO_2 methanation properties over MgO modified Ni/SiO_2 catalysts, Catal. Commun., 54 (2014) 55-60.
[17] Y. Xu, Y. Wu, J. Li, S. Wei, X. Gao, P. Wang, Combustion-impregnation preparation of Ni/SiO_2 catalyst with improved low-temperature activity for CO_2 methanation, Int. J. Hydrogen Energy, 46 (2021) 20919-20929.
[18] J. Yang Lim, J. McGregor, A.J. Sederman, J.S. Dennis, Kinetic studies of CO_2 methanation over a Ni/ γ -Al_2O_3 catalyst using a batch reactor, Chem. Eng. Sci., 141 (2016) 28-45.
[19] Y. Xu, X. Du, L. Shi, T. Chen, H. Wan, P. Wang, S. Wei, B. Yao, J. Zhu, M. Song, Improved performance of Ni/Al_2O_3 catalyst deriving from the hydrotalcite precursor synthesized on Al_2O_3 support for dry reforming of methane, Int. J. Hydrogen Energy, 46 (2021) 14301-14310.
[20] M.M. Millet, G. Algara-Siller, S. Wrabetz, A. Mazheika, F. Girgsdies, D. Teschner, F. Seitz, A. Tarasov, S.V. Levchenko, R. Schlogl, E. Frei, Ni Single Atom Catalysts for CO_2 Activation, J. Am. Chem. Soc., 141 (2019) 2451-2461.
[21] J.M. Crawford, B.E. Petel, M.J. Rasmussen, T. Ludwig, E.M. Miller, S. Halingstad, S.A. Akhade, S.H. Pang, M.M. Yung, Influence of residual chlorine on Ru/TiO_2 active sites during CO2 methanation, Appl. Catal. A: Gen., 663 (2023) 119292.
[22] J. Zhou, Z. Gao, G. Xiang, T. Zhai, Z. Liu, W. Zhao, X. Liang, L. Wang, Interfacial compatibility critically controls Ru/TiO(2) metal-support interaction modes in CO(2) hydrogenation, Nat. Commun., 13 (2022) 327.
[23] F. Ge, J. Zhu, X. Du, P. Wang, Y. Chen, W. Zhuang, M. Song, L. Sun, X. Tao, J. Li, Y. Xu, Constructing the highly efficient Ni/ZrO_2/SiO_2 catalyst by a combustion-impregnation method for low-temperature CO_2 methanation, J. Environ. Chem. Eng., 10 (2022).
[24] J. Tan, J. Wang, Z. Zhang, Z. Ma, L. Wang, Y. Liu, Highly dispersed and stable Ni nanoparticles confined by MgO on ZrO_2 for CO_2 methanation, Appl. Surf. Sci., 481 (2019) 1538-1548.
[25] M. Song, L. Shi, X. Xu, X. Du, Y. Chen, W. Zhuang, X. Tao, L. Sun, Y. Xu, Ni/M/SiO_2 catalyst (M=La, Ce or Mg) for CO_2 methanation: Importance of the Ni active sites, J. CO_2 Util., 64 (2022) 102150.
[26] K. Mette, S. Kühl, A. Tarasov, M.G. Willinger, J. Kröhnert, S. Wrabetz, A. Trunschke, M. Scherzer, F. Girgsdies, H. Düdder, K. Kähler, K.F. Ortega, M. Muhler, R. Schlögl, M. Behrens, T. Lunkenbein, High-Temperature Stable Ni Nanoparticles for the Dry Reforming of Methane, ACS Catal., 6 (2016) 7238-7248.
[27] Y. Song, E. Ozdemir, S. Ramesh, A. Adishev, S. Subramanian, A. Harale, M. Albuali, B.A. Fadhel, A. Jamal, D. Moon, S.H. Choi, C.T. Yavuz, Dry reforming of methane by stable Ni-Mo nanocatalysts on single-crystalline MgO, Science, 367 (2020) 777-781.
[28] M. Jafarbegloo, A. Tarlani, A.W. Mesbah, J. Muzart, S. Sahebdelfar, NiO–MgO Solid Solution Prepared by Sol–Gel Method as Precursor for Ni/MgO Methane Dry Reforming Catalyst: Effect of Calcination Temperature on Catalytic Performance, Catal. Lett., 146 (2015) 238-248.
[29] Y.J.O. Asencios, E.M. Assaf, Combination of dry reforming and partial oxidation of methane on NiO–MgO–ZrO_2 catalyst: Effect of nickel content, Fuel Process. Technol., 106 (2013) 247-252.

[30] P. Hongmanorom, J. Ashok, G. Zhang, Z. Bian, M.H. Wai, Y. Zeng, S. Xi, A. Borgna, S. Kawi, Enhanced performance and selectivity of CO_2 methanation over phyllosilicate structure derived Ni-Mg/SBA-15 catalysts, Appl. Catal. B, 282 (2021) 119564.
[31] M. Romero-Sáez, A.B. Dongil, N. Benito, R. Espinoza-González, N. Escalona, F. Gracia, CO2 methanation over nickel-ZrO_2 catalyst supported on carbon nanotubes: A comparison between two impregnation strategies, Appl. Catal. B, 237 (2018) 817-825.
[32] J. Ren, C. Mebrahtu, L. van Koppen, F. Martinovic, J.P. Hofmann, E.J.M. Hensen, R. Palkovits, Enhanced CO_2 methanation activity over $La_{2-x}Ce_xNiO_4$ perovskite-derived catalysts: Understanding the structure-performance relationships, Chem. Eng. J., 426 (2021) 131760.
[33] R.-P. Ye, L. Liao, T.R. Reina, J. Liu, D. Chevella, Y. Jin, M. Fan, J. Liu, Engineering Ni/SiO2 catalysts for enhanced CO_2 methanation, Fuel, 285 (2021) 119151.
[34] T. Zhang, W. Wang, F. Gu, W. Xu, J. Zhang, Z. Li, T. Zhu, G. Xu, Z. Zhong, F. Su, Enhancing the low-temperature CO_2 methanation over Ni/La-CeO_2 catalyst: The effects of surface oxygen vacancy and basic site on the catalytic performance, Appl. Catal. B, 312 (2022) 121385.
[35] Y. Xu, H. Wan, X. Du, B. Yao, S. Wei, Y. Chen, W. Zhuang, H. Yang, L. Sun, X. Tao, P. Wang, Highly active Ni/CeO_2/SiO_2 catalyst for low-temperature CO_2 methanation: Synergistic effect of small Ni particles and optimal amount of CeO_2, Fuel Process. Technol., 236 (2022).
[36] S. Cisneros, L. Santa-Taborda, L. Martínez Quintana, A.I.M. Rabee, H. Abed, N. Rockstroh, S. Bartling, M. Romero-Sáez, H. Atia, A. Belén Dongil, A. Brückner, J. Rabeah, The effect of O-vacancies on intermediates stability and electron delocalization over MgO modified Ru/ZrO2: Spectroscopic insights during CO_2 methanation, Chem. Eng. J., 474 (2023).
[37] M. Zhu, P. Tian, X. Cao, J. Chen, T. Pu, B. Shi, J. Xu, J. Moon, Z. Wu, Y.-F. Han, Vacancy engineering of the nickel-based catalysts for enhanced CO_2 methanation, Appl. Catal. B, 282 (2021) 119561.
[38] S. Lin, R. Tang, X. Liu, L. Gong, Z. Li, Modulating CO_2 methanation activity on Ni/CeO_2 catalysts by tuning ceria facet-induced metal-support interaction, Int. J. Hydrogen Energy, 51 (2024) 462-475.
[39] F. Wang, S. He, H. Chen, B. Wang, L. Zheng, M. Wei, D.G. Evans, X. Duan, Active Site Dependent Reaction Mechanism over Ru/CeO_2 Catalyst toward CO_2 Methanation, J. Am. Chem. Soc., 138 (2016) 6298-6305.
[40] E. Florez, P. Fuentealba, F. Mondragón, Chemical reactivity of oxygen vacancies on the MgO surface: Reactions with CO_2, NO_2 and metals, Catal. Today, 133-135 (2008) 216-222.
[41] O.E. Everett Espino, P.C. Zonetti, R.R. Celin, L.T. Costa, O.C. Alves, J.C. Spadotto, L.G. Appel, R.R. de Avillez, The tendency of supports to generate oxygen vacancies and the catalytic performance of Ni/ZrO_2 and Ni/Mg(Al)O in CO_2 methanation, Catal. Sci. Technol., 12 (2022) 1324-1338.
[42] P. Huang, J. Chu, J. Fu, J. Yu, S. Li, Y. Guo, C. Zhao, J. Liu, Influence of reduction conditions on the structure-activity relationships of $NaNO_3$-promoted Ni/MgO dual function materials for integrated CO2 capture and methanation, Chem. Eng. J., 467 (2023) 143431.
[43] L.-J. Li, W.-J. Yi, T.-W. Liu, C. Huang, Z.-S. Chao, Hydrogenation of 3-hydroxypropanal into 1,3-propanediol over bimetallic Ru–Ni catalyst, RSC Adv., 7 (2017) 32027-32037.
[44] A. Nagu, K. Vasikerappa, P. Gidyonu, C. Prathap, M. Venkata Rao, K.S. Rama Rao, B. David Raju, Additive-free vapour-phase hydrogenation of benzonitrile over MgO-supported Ni catalysts, RES. CHEM. INTERMEDIAT., 46 (2020) 2669-2681.

[45] Y. Yan, Y. Dai, H. He, Y. Yu, Y. Yang, A novel W-doped Ni-Mg mixed oxide catalyst for CO_2 methanation, Appl. Catal. B, 196 (2016) 108-116.
[46] H. Li, H. Ma, W. Zhao, X. Li, J. Long, Upgrading lignin bio-oil for oxygen-containing fuel production using Ni/MgO: Effect of the catalyst calcination temperature, Appl. Energy, 253 (2019) 113613.
[47] G. Baldauf-Sommerbauer, S. Lux, W. Aniser, B. Bitschnau, I. Letofsky-Papst, M. Siebenhofer, Steady-state and controlled heating rate methanation of CO_2 on Ni/MgO in a bench-scale fixed bed tubular reactor, J. CO_2 Util., 23 (2018) 1-9.
[48] M. Nguyen-Quang, F. Azzolina-Jury, F. Thibault-Starzyk, A. Travert, M. Ziąbka, B. Samojeden, M. Motak, P. Da Costa, Unveiling the potential of surfactant Pluronic-P123 application during the synthesis of Ni-hydrotalcite-derived catalysts for low-temperature CO_2 methanation: A novel approach, Appl. Mater. Today, 32 (2023) 101805.
[49] F. Goodarzi, M. Kock, J. Mielby, S. Kegnæs, CO_2 methanation using metals nanoparticles supported on high surface area MgO, J. CO_2 Util., 69 (2023) 102396.
[50] F. Arena, A. Licciardello, A. Parmaliana, The role of Ni2+ diffusion on the reducibility of NiO/MgO system: A combined TRP-XPS study, Catal. Lett., 6 (1990) 139-149.
[51] R. Pérez-Hernández, A.G. Martínez, G.M. Galicia, M.E. Fernández García, O.C. Nuñez, M.V. Hernández, P. López, C.E. Gutiérrez Wing, Carbon cycle using the CO2 conversion to methane as environmental feasibility on Ni/TiO_2-Na nanotubes catalysts, Renew. Energy, 217 (2023).
[52] M. Jafarbegloo, A. Tarlani, A.W. Mesbah, S. Sahebdelfar, One-pot synthesis of NiO–MgO nanocatalysts for CO_2 reforming of methane: The influence of active metal content on catalytic performance, J. Nat. Gas Eng., 27 (2015) 1165-1173.
[53] V. Danghyan, A. Kumar, A. Mukasyan, E.E. Wolf, An active and stable NiOMgO solid solution based catalysts prepared by paper assisted combustion synthesis for the dry reforming of methane, Appl. Catal. B, 273 (2020) 119056.
[54] Y. Chen, W. Liu, P. Yin, M. Ju, J. Wang, W. Yang, Y. Yang, C. Shen, Synergistic effect between Ni single atoms and acid–base sites: Mechanism investigation into catalytic transfer hydrogenation reaction, J. Catal., 393 (2021) 1-10.
[55] Z. Zuo, S. Liu, Z. Wang, C. Liu, W. Huang, J. Huang, P. Liu, Dry Reforming of Methane on Single-Site Ni/MgO Catalysts: Importance of Site Confinement, ACS Catal., 8 (2018) 9821-9835.
[56] K. Wang, X. Wang, X. Liang, Synthesis of High Metal Loading Single Atom Catalysts and Exploration of the Active Center Structure, ChemCatChem, 13 (2020) 28-58.
[57] B. Jin, S. Li, X. Liang, Enhanced activity and stability of MgO-promoted Ni/Al_2O_3 catalyst for dry reforming of methane: Role of MgO, Fuel, 284 (2021) 119082.
[58] K. Wang, S. Li, M. Yu, X. Liang, Enhancing DMC Production from CO_2: Tuning Oxygen Vacancies and In Situ Water Removal, Energies, 17 (2024).
[59] J. Lefebvre, S. Bajohr, T. Kolb, A comparison of two-phase and three-phase CO_2 methanation reaction kinetics, Fuel, 239 (2019) 896-904.
[60] J.A. Onrubia-Calvo, A. Quindimil, A. Davó-Quiñonero, A. Bermejo-López, E. Bailón-García, B. Pereda-Ayo, D. Lozano-Castelló, J.A. González-Marcos, A. Bueno-López, J.R. González-Velasco, Kinetics, Model Discrimination, and Parameters Estimation of CO_2 Methanation on Highly Active Ni/CeO_2 Catalyst, Ind. Eng. Chem. Res., 61 (2022) 10419-10435.
[61] Z. Bian, Y.M. Chan, Y. Yu, S. Kawi, Morphology dependence of catalytic properties of Ni/CeO2 for CO2 methanation: A kinetic and mechanism study, Catal. Today, 347 (2020) 31-38.

[62] M.-M. Millet, A.V. Tarasov, F. Girgsdies, G. Algara-Siller, R. Schlögl, E. Frei, Highly Dispersed Ni0/$Ni_xMg_{1-x}O$ Catalysts Derived from Solid Solutions: How Metal and Support Control the CO_2 Hydrogenation, ACS Catal., 9 (2019) 8534-8546.
[63] A. Loder, M. Siebenhofer, S. Lux, The reaction kinetics of CO_2 methanation on a bifunctional Ni/MgO catalyst, J. Ind. Eng. Chem., 85 (2020) 196-207.
[64] Y.H. Hu, E. Ruckenstein, Comment on "Dry reforming of methane by stable Ni-Mo nanocatalysts on single-crystalline MgO", Science, 368 (2020).
[65] E. Ruckenstein, Y.H. Hu, Carbon dioxide reforming of methane over nickel/alkaline earth metal oxide catalysts, Appl. Catal. A, 133 (1995) 149-161.
[66] M.-G. Jeong, S.Y. Kim, D.H. Kim, S.W. Han, I.H. Kim, M. Lee, Y.K. Hwang, Y.D. Kim, High-performing and durable MgO/Ni catalysts via atomic layer deposition for CO_2 reforming of methane (CRM), Appl. Catal. A, 515 (2016) 45-50.
[67] Y.-H. Wang, H.-M. Liu, B.-Q. Xu, Durable Ni/MgO catalysts for CO_2 reforming of methane: Activity and metal–support interaction, J. Mol. Catal. A: Chem., 299 (2009) 44-52.
[68] P.A.U. Aldana, F. Ocampo, K. Kobl, B. Louis, F. Thibault-Starzyk, M. Daturi, P. Bazin, S. Thomas, A.C. Roger, Catalytic CO2 valorization into CH4 on Ni-based ceria-zirconia. Reaction mechanism by operando IR spectroscopy, Catal. Today, 215 (2013) 201-207.
[69] Q. Pan, J. Peng, S. Wang, S. Wang, In situ FTIR spectroscopic study of the CO2methanation mechanism on Ni/$Ce_{0.5}Zr_{0.5}O_2$, Catal. Sci. Technol., 4 (2014) 502-509.
[70] A. Aitbekova, L. Wu, C.J. Wrasman, A. Boubnov, A.S. Hoffman, E.D. Goodman, S.R. Bare, M. Cargnello, Low-Temperature Restructuring of CeO(2)-Supported Ru Nanoparticles Determines Selectivity in CO(2) Catalytic Reduction, J. Am. Chem. Soc., 140 (2018) 13736-13745.
[71] B. Jin, K. Wang, H. Yu, X. He, X. Liang, Engineering oxygen vacancy-rich CeO_x overcoating onto Ni/Al_2O_3 by atomic layer deposition for bi-reforming of methane, Chem. Eng. J., 459 (2023) 141611.
[72] B. Jin, S. Li, Y. Liu, X. Liang, Engineering metal-oxide interface by depositing ZrO_2 overcoating on Ni/Al2O3 for dry reforming of methane, Chem. Eng. J., 436 (2022).
[73] X. Ding, Y. Yang, Z. Li, P. Huang, X. Liu, Y. Guo, Y. Wang, Engineering a Nickel–Oxygen Vacancy Interface for Enhanced Dry Reforming of Methane: A Promoted Effect of CeO_2 Introduction into Ni/MgO, ACS Catal., 13 (2023) 15535-15545.